Malaysian Journal of Chemical Engineering & Technology

Dual phase zirconium-based metal-organic gel (Zr-MOG) as chromium (VI) removal via photoreduction

[a,b]Anis Muneerah Shaiful Bahari, [c]Nurhaswani Alias, [c]Siti Azlina Rosli, [c]Nurliyana Abu Hasan Sazalli,

[c]Zainovia Lockman, [a]Halina Misran*

[a]Nanoarchitectonic Laboratory, Department of Mechanical Engineering, Universiti Tenaga Nasional, Selangor, Malaysia
[b]Material Engineering & Testing Group, TNB Research Sdn Bhd, Selangor, Malaysia
[c]School of Materials and Mineral Resources Engineering, Universiti Sains Malaysia, Penang, Malaysia

*Corresponding email: Halina@uniten.edu.my

Abstract

Given the widespread production of Cr(VI) from numerous industrial processes, as well as its harmful toxicity as a carcinogenic agent, it is critical to explore stable and efficient adsorbents with quick performance for Cr(VI). Recently, environmentally friendly adsorbents have been employed to reduce metallic pollutants in aqueous media called zirconium-containing metal-organic frameworks (Zr-MOFs) or UiO-66. UiO-66 are favourable because of their nontoxic metal sources, outstanding stabilities, and distinctive physicochemical characteristics. Despite the benefits of using MOFs, overcoming their poor macro-shaping and hydro-stability to be used as commercial adsorbents and catalysts remains a significant problem. Zirconium-based metal-organic gel (Zr-MOG) xerogel is widely known as a new nanomaterial to overcome metal-organic framework (MOFs) disadvantage as microcrystalline powder. This research is an effort to investigate green Zr-MOG as a potential photocatalyst for reducing Cr(VI) to Cr(III) ions. The behaviour of Zr-MOG in dark adsorption and photocatalysis, with and without a scavenger, as well as its reusability were studied. Besides that, synthesised Zr-MOG xerogel exhibited three different X-ray diffraction (XRD) pattern categories: fully amorphous, 1:1 ratio and 1:4 ratio of amorphous and crystalline structure. The performance of pure amorphous MOG, pure crystalline MOG and dual-phase MOG as photocatalysts were compared. The dual-phase structure Zr-MOG 5 exhibits the greatest Cr(VI) ion reduction, with an 87% removal rate in 120 minutes.

Article Info

1.0 Introduction

Industrial activities are now required to meet human demands. Due to the toxins that are released into the environment, the growth of industrial sectors has a negative impact on the ecosystem. Heavy metals found in industrial effluent are a frequent hazard that can contaminate drinking water. According to the Global Burden of Disease Study 2019 (GBD2019), India has the highest death rate in Asia, with over 79,000 deaths caused by contaminated water sources. This circumstance brings up scientific and general concerns regarding human health. Fig. 1 shows the death rate from unsafe water sources in relation to the share of the population living in extreme poverty, focusing on Asia, which was published in 2020. Besides that, it was reported that the uncontrolled

dispersion of heavy metals into the receiving environment from a variety of industrial, residential, agricultural, medical, and technical application fields produces pollution (Nuclear Energy Agency, 2015; Lv et al., 2019; Rajeshkumar et al., 2018). Due to their toxicity, resistance to degradation, carcinogenicity, and teratogenicity, heavy metals like arsenic (As), cadmium (Cd), chromium (Cr), lead (Pb), and mercury (Hg) pose a serious threat to the ecosystem (Kobielska et al., 2018; Rosli et al., 2021).

Chromium (VI), a carcinogen, genotoxic agent, and one of the most concerning pollutants in aquatic environments, is produced by a variety of industrial activities (Costa, 2003; Pakade et al., 2019; Rosli et al., 2021; Shokouhfar et al., 2018). Detoxification of Cr(VI) contaminated water has so been a recent research interest (Noraee et al., 2019; Shokouhfar et

al., 2018; Wani et al., 2018). One of the requirements for Cr(VI) adsorption in industry is high stability of an adsorbent across a broad pH range. Thus, metal-organic framework (MOF) is a potential adsorbent for Cr(VI) (Shokouhfar et al., 2018).

Previously, UiO-66 had shown a significant performance as Cr removal. Most of the previous studies on UiO-66 focused on removing Cr(III) (Wen et al., 2018). However, in 2018, Shokouhfar et al. reported a high adsorption capacity (60.24 mg g^{-1}) and a quick adsorption rate (3 min) for the adsorption of Cr(VI) oxo-anion species in aqueous solutions using modified UiO-66 (TMU-66). Furthermore, Shaiful Bahari et al. (2021b) and Jiang et al. (2020) had also explored on using UiO-66 as photocatalyst in reducing Cr(VI) to Cr(III). Both studies reported more than 45% of Cr(VI) removal efficiency were achieved.

MOFs have garnered a lot of interest in water treatment in recent years because of their enormous specific surface area, rich pore structure, and excellent chemical stability (Kobielska et al., 2018; Pinto et al., 2013). However, the aggregation in MOFs particles unavoidably happened due to the nature of the crystalline powder, resulting in a decreased valid surface area (Yang et al., 2023). Furthermore, MOFs are challenging to manufacture and form, which further restricts the scope of their use. Metal organic

gels (MOGs) are the twinborn counterpart of MOFs and are produced using the same precursors (Santos-Lorenzo et al., 2019). Crystallographic analysis reveals distinct structural regularity with the corresponding MOFs, which display a three-dimensional (3D) porous structure made of metal ions and organic ligands through a variety of affinities, including coordination interaction, hydrophobic interaction, and H-bonding (Yang et al., 2023). Without using a binder, this flexible material can be arbitrarily shaped into appealing shapes to meet demands for different situations (Abánades Lázaro & Forgan, 2019; Huskić et al., 2019; Shokouhfar et al., 2018; Valvekens et al., 2013). Due to their ease of recycling, good shape ability and lower density, MOGs have a more favourable outlook in the field of wastewater treatment than MOFs (Yang et al., 2023). Additionally, the amorphous material is metastable, and the disorder in the framework during the electrochemical test, such as in the use of supercapacitors, will result in more active sites (Yang et al., 2018). However, most of the previous research on MOF or MOG has focused on either a fully crystalline MOF or a fully amorphous MOG. On the other hand, the development of dual-phase materials has been slowly growing to reveal the underlying mechanisms involved and the potential applications. Dual phase materials can have both amorphous and
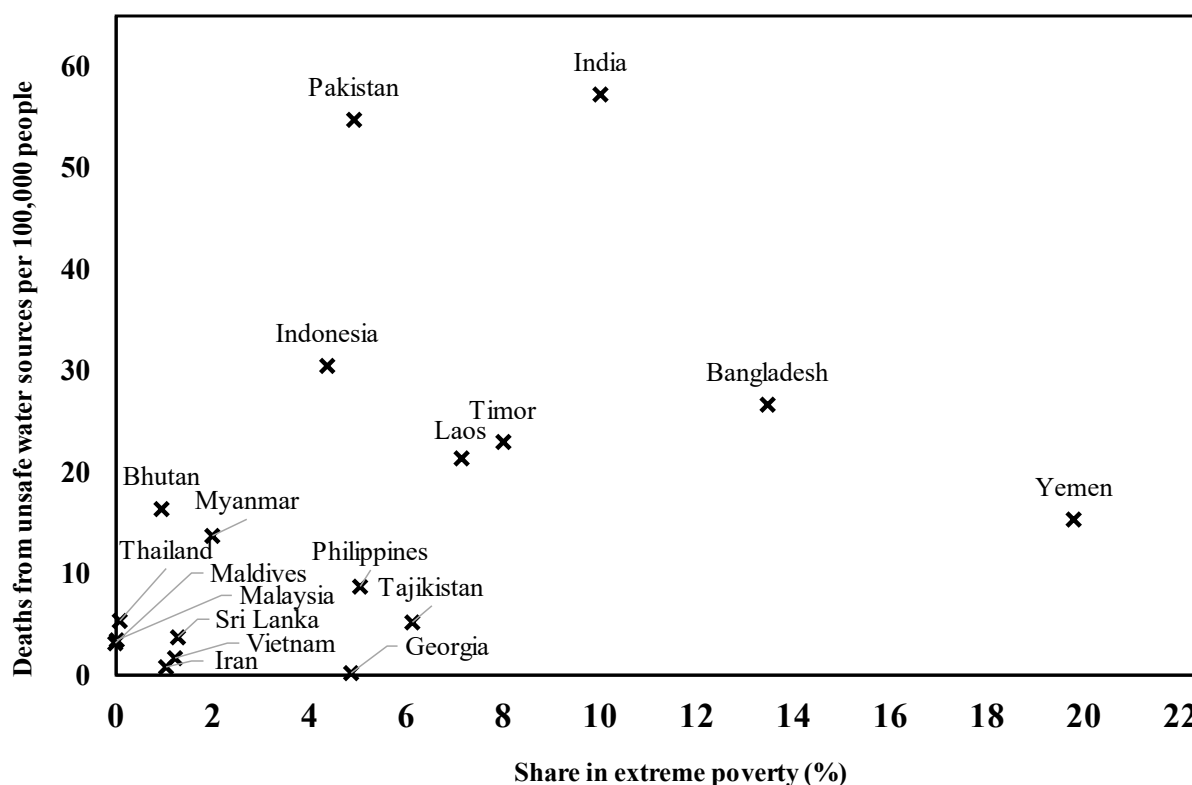

Fig. 1: The reported death rate from unsafe water sources in Asia (Institute for Health Metrics and Evaluation (IHME), 2021)

crystalline phases, which have unique properties that are not found in either pure amorphous or pure crystalline materials (Chen et al., 2021). For example, dual phase materials can exhibit improved mechanical, thermal, and optical properties compared to pure amorphous or crystalline materials and have potential applications in a variety of fields, including electronics, energy storage and catalysis (Chen et al., 2021).

Therefore, in this study, the characteristic of synthesised dual-phase Zr-based MOGs by Shaiful Bahari et al. (2021a) were discussed further and the usage of Zr-MOG as photocatalyst for photoreduction of Cr(VI) ions from water were also elucidated. The structural analysis of differences in high-resolution transmission electron microscopy (HRTEM) and X-ray diffraction (XRD) analysis was described. Additionally, the behaviours and performance of Cr(VI) removal using Zr-MOG as a photocatalyst were discussed.

2.0 Methodology

2.1 Synthesis

In this study, the samples were synthesised using zirconium (IV) oxynitrate, ($ZrO(NO_3)_2 \cdot xH_2O$, Fluka), terephthalic acid ($C_8H_6O_4$,1,4-benzenedicarboxylic acid, H_2BDC, Merck, 98%), ethanol absolute (synthesis grade, C_2H_5OH, HmbG Chemicals) as well as distilled deionised water as mentioned in previous study (Shaiful Bahari et al., 2021a). All reagents were obtained commercially and used without further purification.

The samples undergo mixing, aging, centrifuge, and drying. The parameters used in the synthesis method are as shown in Table 1. In this study, 4 samples from the previous study by Shaiful Bahari et al. (2021a) were selected. Zr-MOG 3, Zr-

Table 1: Synthesis parameters for Zr-MOG 1, Zr-MOG 3, Zr-MOG 4 and Zr-MOG 6 (Shaiful Bahari et al., 2021a)

Sample	Mixing method	Aging	Drying
Zr-MOG 3	Stir 24 h	-	90 °C for 12 h
Zr-MOG 4	Stir 6 h	-	90 °C for 12 h
Zr-MOG 5	Stir 48 h	-	90 °C for 12 h
Zr-MOG 6	Stir 24 h	140 °C for 24 h	110 °C for 24 h

MOG 4, Zr-MOG 5, and Zr-MOG 6 were selected for Cr(VI) removal application. The selections were made based on different XRD pattern category. Zr-MOG 3, Zr-MOG 4, Zr-MOG 5, and Zr-MOG 6 were chosen to represent the three categories of the XRD pattern. Zr-MOG 3 and Zr-MOG 4 were chosen from the same category to compare the removal efficiency produced by similar XRD patterns.

2.2 Characterisations

In this study, structural characterisations such as XRD and HRTEM were elaborated in detail as additional data from previous article (Shaiful Bahari et al., 2021a). XRD (Shimadzu XRD-6000) with CuKα radiation of 1.5406 Å was used. The scan step and speed used were 0.020 and 3°/min, respectively. The angle used are in range of $2\theta = 5°$ to $45°$. The respective voltage and current employed are 30 kV and 20 mA (Fadli et al., 2019; Mahadi et al., 2015). High-resolution transmission electron microscopy (HRTEM) analysis was done using TECNAI G2 F20 X-Twin manufactured by FEI at 200 kV. Zr-MOG was dissolved in ethanol to prepare the samples, which were then sonicated for 15 minutes. Grids with carbon coatings were placed on the specimen holder after being dipped into the resulting solution. HRTEM and Selected Area Electron Diffraction (SAED) mainly record structural information (Zhao et al., 2016). It can directly identify a crystal structure (Gökpinar et al., 2019). Zr-MOG 3 and Zr-MOG 6 were chosen to compare the different structures as suggested in XRD analysis.
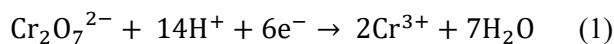
2.3 Photoreduction of Cr(VI) ions from aqueous solution

Potassium dichromate ($K_2Cr_2O_7$) was dissolved in deionised water to create Solution 1 of Cr(VI), which contained 100 ppm of Cr(VI) and had an initial pH of 4. Then, to create Solution 2, Solution 1 was further diluted to 5 ppm and the pH was brought down to 2 by adding HCl. The sample powders were placed in tea bags with 25 mL of Solution 2. The sample in Solution 2 was placed in the dark for approximately 30 minutes prior to light irradiation to reach adsorption-desorption equilibrium. After that, the mixture was exposed to ultraviolet (UV) light for 120 minutes. By removing 5 mL of Solution 2 at 30-minute intervals, the concentration of Cr(VI) present was collected. Following that, UV-visible spectroscopy (Perkin Elmer Lambda 35) was used to measure the solution's UV absorbance at 350 nm.

According to Eq. (1) (Shokouhfar et al., 2018), extra electrons are required for the complete reduction of Cr(VI) to Cr(III) ion.

$$Cr_2O_7^{2-} + 14H^+ + 6e^- \rightarrow 2Cr^{3+} + 7H_2O \quad (1)$$

The estimated removal efficiency, R (%) was calculated according to Eq. (2) (Noraee et al., 2019).

$$R\ (\%) = (C_0 - C_t)/C_0 \quad (2)$$

where C_o and C_t are the initial and final concentrations in mg/L of Cr(VI) ions, respectively. UV light was employed specifically for the purpose of photoreduction of Cr(VI) ions from aqueous solutions. The energy of the UV light (Hitachi F8T5-Black Light, 8 Watts) employed was 3.4 eV, which is larger than the band gap of the UiO-66 material (3.05 eV) (Li et al., 2018). Photogenerated are to be anticipated. The pseudo-first-order Langmuir Hinshelwood model was used to compute the reaction kinetic (Rosli et al., 2021).

$$R = -dC/dt = kt \quad (3)$$

In the case of weak adsorption, this can be written as:

$$-\ln(C/C_0) = kt \quad (4)$$

where C is the concentration of Cr(VI) at the given time, R is the photocatalytic reaction rate, k is the photocatalytic pseudo-first order reaction rate constant, and C_o is the initial concentration of Cr(VI).

3.0 Results and discussion

3.1 Characterisations

Fig. 2 shows all XRD analysis for Zr-MOG obtained at $2\theta = 5°$ to $45°$. All xerogels displayed a broad peak at $2\theta = 6°$ to $10°$ centred at approximately $2\theta = 8°$, demonstrating that Zr-MOG successfully formed (Bueken et al., 2020; Connolly et al., 2019; Li et al., 2013; Santos-Lorenzo et al., 2019; Shaiful Bahari et al., 2021a). In contrast to other Zr-MOG, Zr-MOG 6 revealed a totally amorphous structure, suggesting that.

Zr-MOG was successfully formed. XRD patterns of Zr-MOG 3, Zr-MOG 4 and Zr-MOG 5 show distinct peaks at ca. $2\theta = 17.5°$, $25.5°$, and $28°$ were found. These peaks corresponded to the (004), (006),
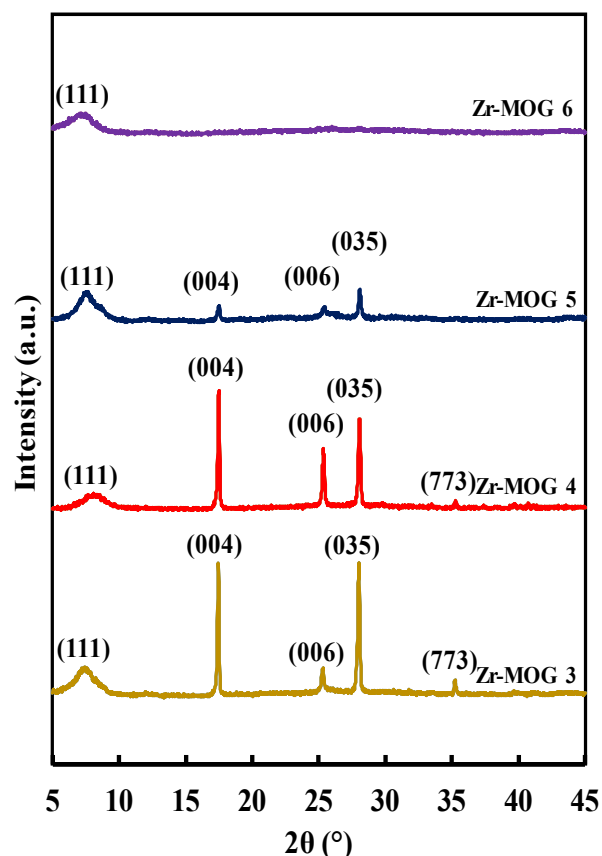

Fig. 2: X-ray diffraction patterns of Zr-MOG synthesised using non-toxic modulator (Shaiful Bahari et al., 2021a)

and (035) reflection planes often seen in the UiO-66 crystalline structure (Cavka et al., 2008). Additionally, Zr-MOG 3 and Zr-MOG 4 showed additional peaks at $2\theta = 35.2°$ associated with the (773) reflection plane. This peak may be a reference to isolated ZrO_2 single crystals (baddeleyite, JCPDS 27-0997) that are not forming a metal-framework structure due to insufficient gelation (Shaiful Bahari et al., 2021a).

It was observed that the synthesised Zr-MOG had 3 distinct XRD patterns. As indicated in Table 2, the patterns are separated into three categories: category 1 (totally amorphous), category 2 (amorphous to crystalline phase ratio is 1:1), and category 3 (amorphous to crystalline size ratio is 1:4). By comparing the intensities of representative amorphous peak and crystalline peak, which contribute to the (111) and (004) crystal planes, respectively, the ratio was calculated. Category 1 of XRD pattern is Zr-MOG 6. Zr-MOG 5 is in Category 2. Finally, category 3 includes Zr-MOG 3 and Zr-MOG 4. Each of the chosen category representatives opted for Cr(VI) removal by photoreduction.
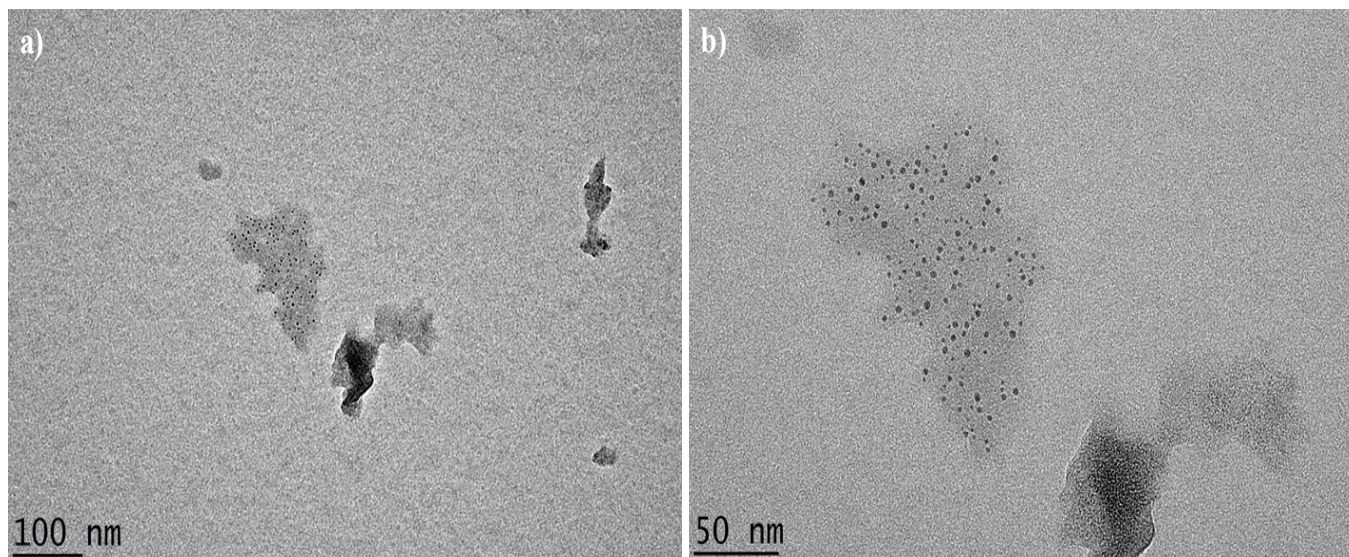
Fig. 3: High resolution transmission electron microscopy (HRTEM) image (scale bar = 100 nm & 50 nm) of xerogel
Zr-MOG 3 particle

Table 2: XRD pattern category of synthesised Zr-MOG

Zr-MOG	Category
3	1:4 (ratio of amorphous and crystalline)
4	1:4 (ratio of amorphous and crystalline)
5	1:1 (ratio of amorphous and crystalline)
6	Fully amorphous

XRD pattern analysis indicated that various conditions in the synthesis of Zr-MOG without toxic modulators can result in dual-phase structures in the material (amorphous and crystalline). Additionally, it is believed that in order to cause amorphisation, the aging and drying temperature must be higher than 100 °C (Bennett & Cheetham, 2014). The XRD patterns of Zr-MOG 3, Zr-MOG 4 and Zr-MOG 5 indicate the development of both crystalline and amorphous material. Based on the previous research and diffract Eva, new peaks were discovered, and it was hypothesised that all the extra peaks were caused by ZrO_2 produced in Zr-MOG (Shaiful Bahari et al., 2021a).

According to XRD research, Zr-MOG 3 had a 1:4 amorphous to crystalline structure ratio, whereas Zr-MOG 6 had a fully amorphous structure. High-resolution TEM images of xerogel Zr-MOG 3 created using the chloride-free method are shown in Fig. 3. Fig. 4 shows the comparison of Selected Area (electron) diffraction (SAED) of Zr-MOG 6 and Zr-MOG 3.

The black particle in Fig. 3 is a Zr-MOG 3 particle, and it is less than 500 nm. A flaky, asymmetrical-shaped particle is observed in Zr-MOG. The thickness of the particles creates the dark contrast (Albers et al., 2015). Most of the particles in the HRTEM image of Zr-MOG 3 are amorphous, but there are also some free-standing crystalline nanoparticles. It was hypothesised that zirconia nanoparticles smaller than 5 nm were created in the reactor as cubic zirconia changed from tetragonal zirconia at normal temperature. The crystalline nanoparticles are clearly free-standing and vary in size. According to its XRD pattern, Zr-MOG 3 is thought to be both an amorphous and crystalline material (Mohan et al., 2015). This type of condition is known as a dual-phase material or a nanocomposite. In these materials, the amorphous and crystalline phases are present in the same sample, often in the form of small crystalline regions within a larger amorphous matrix which is similar to Zr-MOG 3 condition (Kampouri et al., 2018). The exact proportions of each phase can vary, and the arrangement of the two phases can also vary depending on the processing conditions used to create the material.

It was observed in Fig. 4, Zr-MOG 6 particle is larger than Zr-MOG 3. Similar to Zr-MOG 3, which has a flaky asymmetrical shape, Zr-MOG 6 particles have a similar appearance. The main difference is the primary crystallites that are formed in Zr-MOG 3, which has an amorphous and crystalline phase, however, there are no physical grain or phase boundaries in Zr-MOG 6 (Albers et al., 2015). HRTEM images of Zr-MOG 6 can be compared to

those of precipitated silica or silica aerogel, neither of which show any indication of discrete crystalline development inside the amorphous structure (Albers et al., 2015). It was suggested that Zr-MOG 6 is a fully amorphous material.

To support HRTEM images of Zr-MOG 6 and Zr-MOG 3, the inset in Fig. 4 was used to analyse the Selected Area Electron Diffraction (SAED). Based on the ring that is created, SAED can determine the phase in the material. A diffused ring was created by the diffraction pattern in Fig. 4 (b), which indicated the formation of an amorphous phase (Shaiful Bahari et al., 2021a; Wiktor et al., 2017; Yang et al., 2018). On the other hand, Zr-MOG 3 displayed a noticeable halo ring, which showed the material's identified crystalline form (Wiktor et al., 2017). In conclusion, the XRD patterns that suggested its phase are supported by HRTEM and SAED of Zr-MOG 3 and Zr-MOG 6. According to XRD patterns, HRTEM, and SAED, Zr-MOG 3 is a material containing both crystalline and amorphous phases, whereas Zr-MOG 6 is completely amorphous.

3.2 Photoreduction of Cr(VI) ions from aqueous solution

Fig. 5 (a) shows the removal efficiency of Cr(VI) ion by Zr-MOG 6 by dark adsorption and photocatalysis. The photocatalysis process was conducted utilising UV light as the primary source. The removal was carried out both in the absence of light (dark adsorption) and with UV light (photoreduction). The outcome demonstrates that photoreduction outperforms dark adsorption in terms of removal efficiency. Since more photons and electron-hole pairs can be generated in the materials, the light intensity increases the removal efficiency (Lin et al., 2016). The correlation between light intensity and removal effectiveness is according to the previous study (Lin et al., 2016). So, in this investigation, photoreduction was employed.

Fig. 5 (b) shows the removal efficiency of Cr(VI) ion of Zr-MOG 5 by photocatalysis with
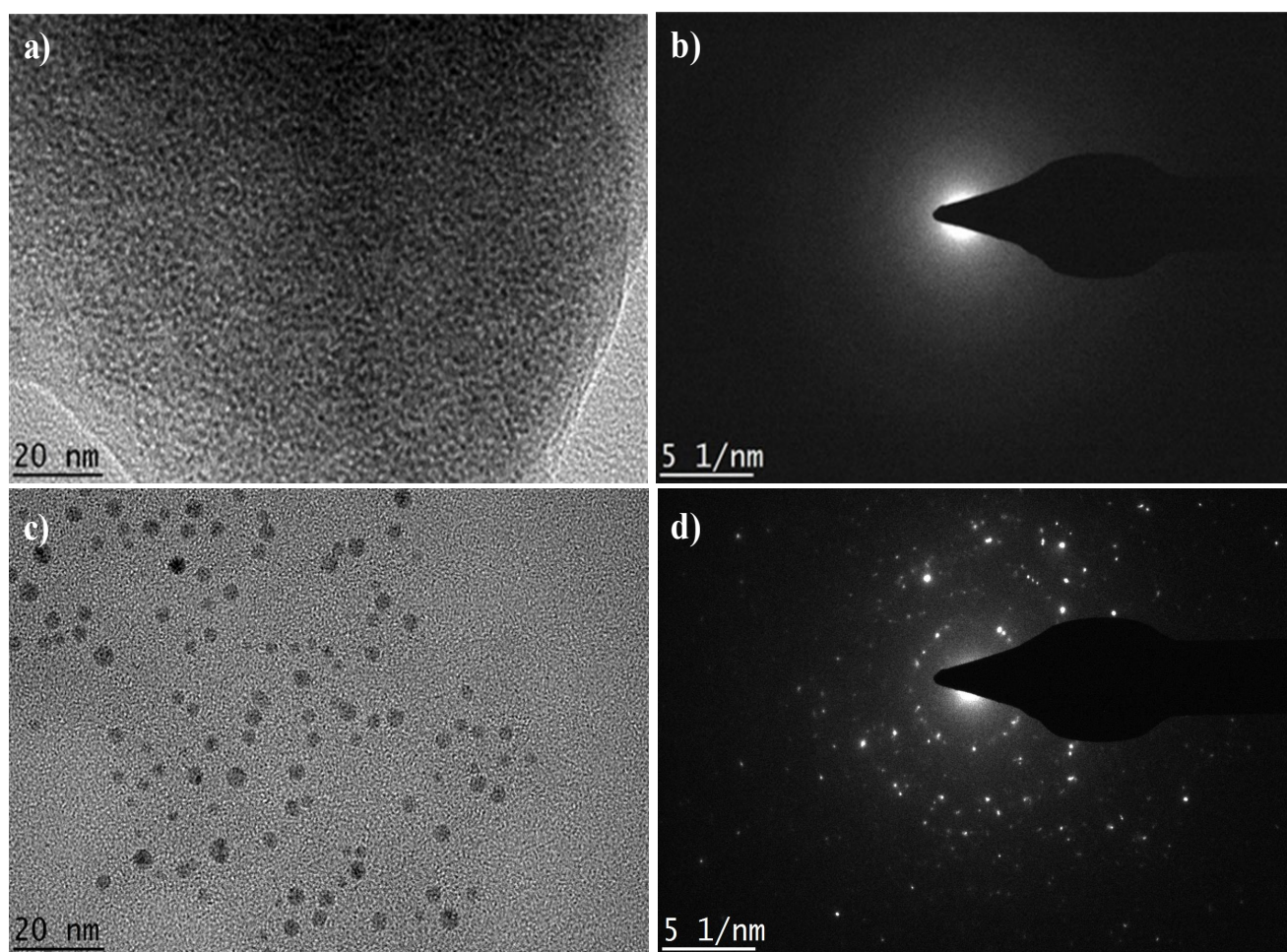

Fig. 4: (a) High Resolution Transmission Electron Microscopy image (scale bar = 20 nm) of amorphous xerogel Zr-MOG 6 particle (Shaiful Bahari et al. 2021a) (b) SAED pattern on the aggregate xerogel Zr-MOG 6 particle (c) High Resolution Transmission Electron Microscopy image (scale bar = 20 nm) of hybrid xerogel Zr-MOG 3 particle (d) SAED pattern on the aggregate xerogel Zr-MOG 3 particle

ethylenediaminetetraacetic acid (EDTA) or without EDTA. It was investigated whether scavengers like ethylenediaminetetraacetic acid (EDTA) were needed for Zr-MOG. In order to improve and stabilise the removal efficiency during photocatalysis reduction, radical scavengers were frequently used (Torbina et al., 2019). The removal efficiency of Cr(VI) ion, in contrast, demonstrated a better removal efficiency without EDTA than with EDTA. A radical chain scavenger is not necessary for Zr-based MOF or MOG to carry out the process of photocatalysis, according to a prior work by Torbina et al. (2019). In this study, photocatalysis reduction is applied to all the samples without the use of a scavenger.

Fig. 5 (c) shows the comparison photoreduction of Cr(VI) ion by Zr-MOG 6 and reuse Zr-MOG. The primary goal for this testing is to evaluate its reusability. The used Zr-MOG was tested once more without washing after being placed in an empty, sealed beaker for the night. Reused Zr-MOG 6

exhibits greater removal effectiveness than the initial test. It demonstrates that the catalyst may be recycled up to twice without losing its functionality or selectivity and that its structural integrity is maintained. This might be a result of the stable Zr-O bond structure in the material (Torbina et al., 2019).

Fig. 6 (a) shows that in 120 minutes, Zr-MOG 3, Zr-MOG 4, Zr-MOG 5, and Zr-MOG 6 removed 36%, 31%, 87%, and 22% of Cr(VI) ions, respectively. In terms of the percentage of Cr(VI) ion removal after 120 minutes, Zr-MOG 3 and Zr-MOG 4 (both of which exhibit similar XRD patterns of category 3) are similar. Zr-MOG 6, on the other hand, which is fully amorphous, exhibits the lowest rate of Cr(VI) ion removal, 22%. Finally, Zr-MOG 5, a sample with a 1:1 ratio of amorphous and crystalline phase, exhibits the highest Cr(VI) removal at about ca. 87% reduction. Fig. 6 (b) shows the kinetic models of Cr(VI) reduction (refer Eq. (4)) by Zr-MOG.
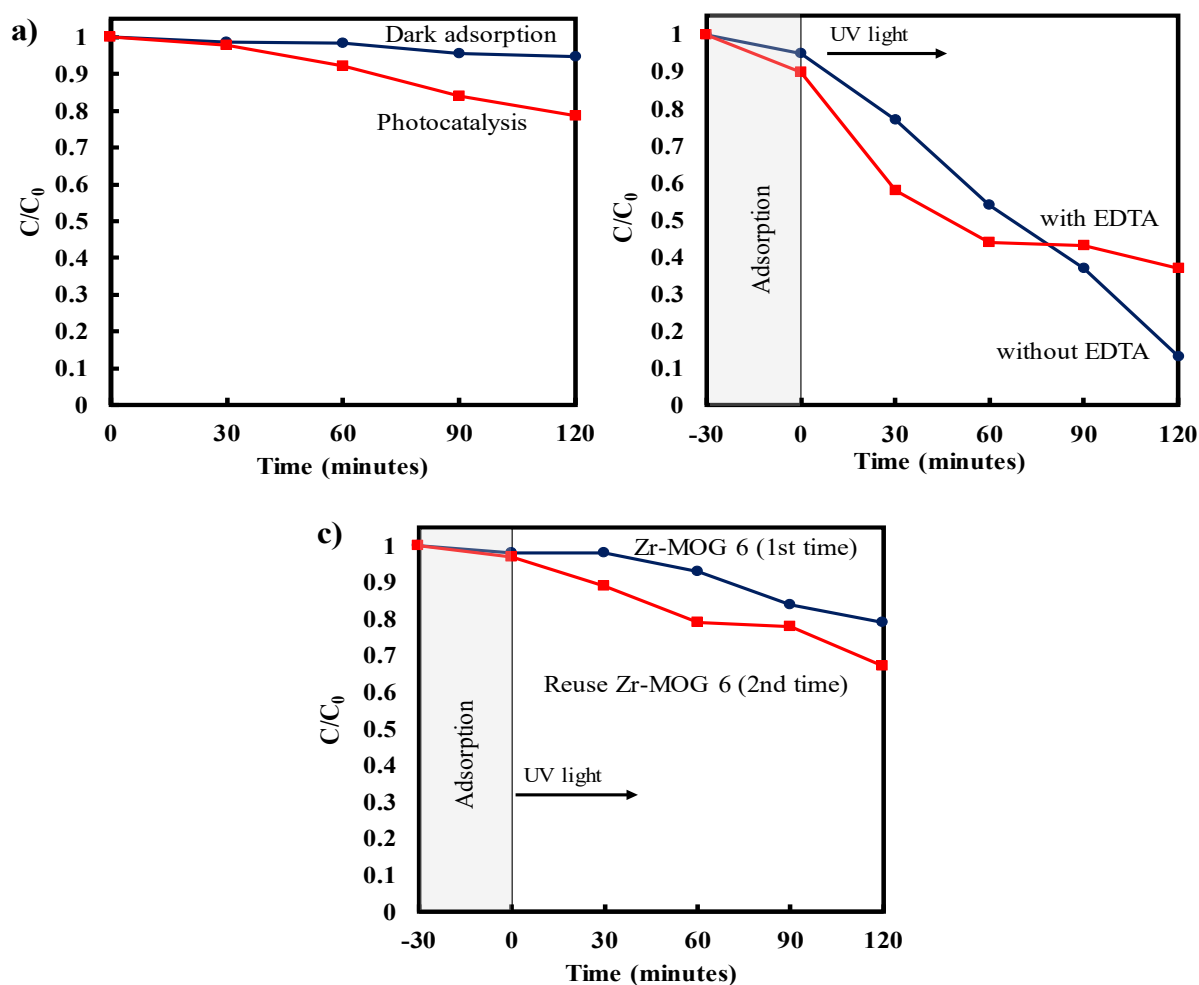

Fig. 5: (a) photoreduction efficiency of Cr(VI) ion by Zr-MOG 6 using dark adsorption and photocatalysis, (b) photoreduction efficiency of Cr(VI) ion of Zr-MOG 5 by photocatalysis with ethylenediaminetetraacetic acid (EDTA) or without EDTA, and (c) comparison photoreduction efficiency of Cr(VI) ion by Zr-MOG 6 and reuse Zr-MOG 6removal efficiency of Cr(VI) by UiO-66 (5) in dark
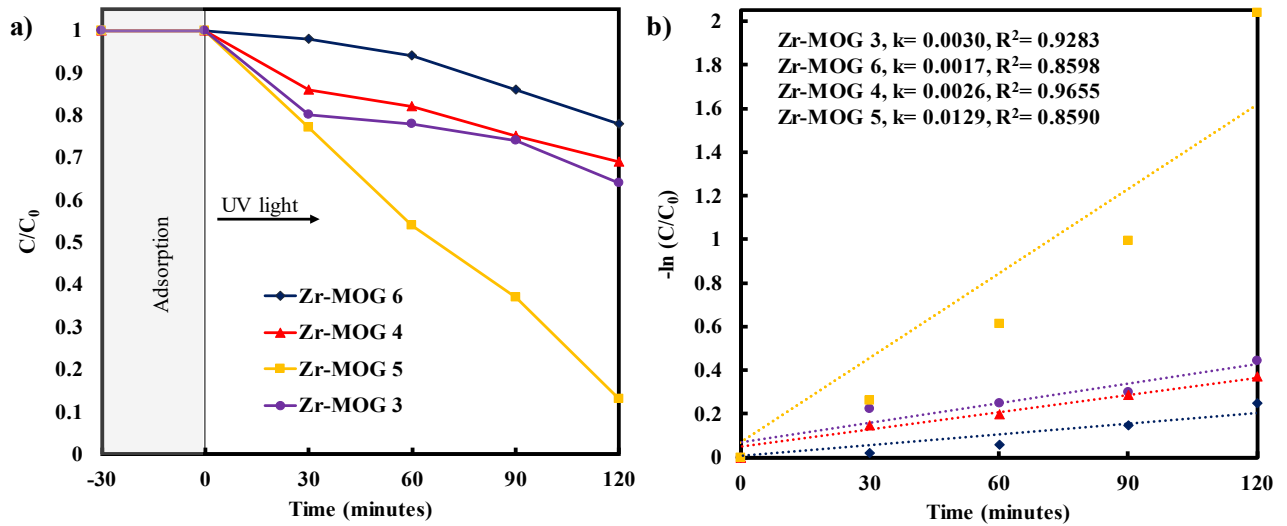
Fig. 6: (a) photoreduction efficiency of Cr(VI) ion removal by Zr-MOG 3, Zr-MOG 4, Zr-MOG 5 and Zr-MOG 6, (b) graph of $-\ln(C/C_o)$ vs. time and the reduction rate constants for Zr-MOG 3, Zr-MOG 4, Zr-MOG 5 and Zr-MOG 6

The values of the correlation coefficient of determination (R^2) and the photocatalytic pseudo-first-order reaction rate (k) for Cr(VI) ions are shown in the insets. R^2 values and constant k values were calculated. The slope of the linear fit is given by the value of k. R^2 must be near to 1, which signifies that the model is appropriate for illustrating Cr(VI) kinetics.

Based on the value of k found in Fig. 6 (b), the photocatalytic reaction of Zr-MOG 5 at k = 0.0129 min^{-1} is almost ten times effective than Zr-MOG 6 at k = 0.0017 min^{-1}. Zr-MOG 3 and Zr-MOG 4 (both of which had an identical XRD pattern) showed a near value of the photocatalytic reaction, with k = 0.0030 min^{-1} and k = 0.0026 min^{-1}, respectively. Zr-MOG with the presence of 2 different phases (amorphous and crystalline) exhibited a better photocatalytic reaction compared to a fully amorphous Zr-MOG. Furthermore, Zr-MOG 5 with a ratio of 1:1 amorphous and crystalline shows a higher efficiency compared to Zr-MOG 3 and Zr-MOG 4 with a ratio of 1:4 amorphous and crystalline structure. The presence of different phases and its ratio effect the performance of Zr-MOG as photocatalyst.

Table 3 shows the comparison of Cr(VI) ion removal by Zr-MOG and UiO-66 from the previous study (Shaiful Bahari; et al., 2021b). UiO-66 (4) exhibits the least amount of Cr(VI) ion elimination in two hours. The elimination efficiency of UiO-66 (1) and UiO-66 (4) is less than 10%. Zr-MOG 6 came next, which removed 22% of the Cr(VI) ions. The removal efficiency of Zr-MOG in category 3

Table 3: The comparison photoreduction of Cr(VI) ion by Zr-MOG and UiO-66 (Shaiful Bahari et al. 2021b) at 120 minutes

Time/ samples	120 minutes
Zr-MOG 3	36%
Zr-MOG 4	31%
Zr-MOG 5	87%
Zr-MOG 6	22%
UiO-66 (1)	8%
UiO-66 (4)	7%
UiO-66 (5)	37%

(Zr-MOG 3 and Zr-MOG 4) is about 30%. The highest Cr(VI) removal efficiency is demonstrated by Zr-MOG 5 with 87% removal in 2 hours. In comparison to the earlier works, this hybrid amorphous/crystalline MOG (Zr-MOG 5) exhibits a greater removal efficiency (Shaiful Bahari et al., 2021b; Noraee et al., 2019).

4.0 Conclusion

Zr-MOG using nitrate-based Zr salt and new green sol-gel method without using HCl as modulator has been successfully synthesised. XRD pattern in Zr-MOG showed three different patterns. HRTEM was employed to identify the phase where the image and SAED showed that Zr-MOG 6 had successfully produced fully amorphous material. However, some synthesised Zr-MOG XRD patterns showed extra

crystalline peaks, suggesting the formation of a structure that is both amorphous and crystalline. HRTEM images showing amorphous particles with free-standing zirconia nanoparticles were associated with the dual-phase structure. Additionally, SAED findings indicated that Zr-MOG 3 may have a dual-phase structure since a prominent ring formed in some locations. The performance of UiO-66 and Zr-MOG in Cr(VI) ion removal from aqueous solution were studied and compared. Zr-MOG demonstrates how various XRD patterns impact the removal efficiency. The maximum removal efficiency of 87% of Cr(VI) ion in two hours is demonstrated by Zr-MOG 5 with a dual-phase structure. The presence of two distinct phases in the structure—amorphous and crystalline—could explain the high removal effectiveness.

Contribution statement

Anis Muneerah Shaiful Bahari: Conceptualisation, methodology, formal analysis, investigation and writing-original draft; **Nurhaswani Alias**: Conceptualisation, methodology, and formal analysis; **Siti Azlina Rosli**: Formal analysis; **Nurliyana Abu Hasan Sazali**: Conceptualisation, methodology, and formal analysis; **Zainovia Lockman**: Conceptualisation, formal analysis, and validation; **Haslina Misran**: Conceptualisation, supervision, writing- review and editing, and validation.

Conflict of Interest

The authors declare that they have no known competing financial interests or personal relationships that could have appeared to influence the work reported in this paper.

Acknowledgement

References

Abánades Lázaro, I., & Forgan, R. S. (2019). Application of zirconium MOFs in drug delivery and biomedicine. *Coordination Chemistry Reviews*, *380*, 230–259. https://doi.org/10.1016/j.ccr.2018.09.009

Albers, P., Maier, M., Reisinger, M., Hannebauer, B., & Weinand, R. (2015). Physical boundaries within aggregates - Differences between amorphous, para-crystalline, and crystalline Structures. *Crystal Research and Technology, 50*(11), 846–865. https://doi.org/10.1002/crat.201500040

Bennett, T. D., & Cheetham, A. K. (2014). Amorphous metal−organic frameworks. *Accounts of Chemical Research, 47*(5), 1555–1562. https://doi.org/10.1021/ar5000314

Bueken, B., Velthoven, N. V., Willhammar, T., Stassen, I., Keen, D. A., Baron, G. V., Joeri, F. M., Ameloot, R., Bals, S., Vos, D. De, & Thomas, D. (2020). Gel-based morphological design of zirconium metal-organic frameworks supporting info. *Chemical Science, 8*(5), 1–14. https://doi.org/10.1039/C6SC05602D

Cavka, J. H., Jakobsen, S., Olsbye, U., Guillou, N., Lamberti, C., Bordiga, S., & Lillerud, K. P. (2008). A new zirconium inorganic building brick forming metal organic frameworks with exceptional stability. *Journal of the American Chemical Society, 130*(42), 13850–13851. https://doi.org/10.1021/ja8057953

Chen, M., Long Z., Gang W., Jun G., Liuxiao L., Qiyuan H., Ye C. & Hua Z. (2021). Phase engineering of metal-organic frameworks. *Aggregate 3*(1), 1–5. https://doi.org/10.1002/agt2.145

Connolly, B. M., Aragones-Anglada, M., Gandara-Loe, J., Danaf, N. A., Lamb, D. C., Mehta, J. P., Vulpe, D., Wuttke, S., Silvestre-Albero, J., Moghadam, P. Z., Wheatley, A. E. H., & Fairen-Jimenez, D. (2019). Tuning porosity in macroscopic monolithic metal-organic frameworks for exceptional natural gas storage. *Nature Communications, 10*(1), 1–11. https://doi.org/10.1038/s41467-019-10185-1

Costa, M. (2003). Potential hazards of hexavalent chromate in our drinking water. *Toxicology and Applied Pharmacology, 188*(1), 1–5. https://doi.org/10.1016/S0041-008X(03)00011-5

Fadli, M. F. M., Misran, H., Othman, S. Z., Bahari, A. M. S., Samsudin, N. A., Rosli, S. A., Lockman, Z., Matsumoto, A., & Amin, N. (2019). Room temperature synthesis and characterizations of CU-MOF using natural polysaccharide as potential organic linker. *International Journal of Recent Technology and Engineering, 8*(4), 6490–6498. https://doi.org/10.35940/ijrte.D5163.118419

Gökpinar, S., Ernst, S. J., Hastürk, E., Möllers, M., El Aita, I., Wiedey, R., Tannert, N., Nießing, S., Abdpour, S., Schmitz, A., Quodbach, J., Füldner, G., Henninger, S. K., & Janiak, C. (2019). Air-con metal-organic frameworks in binder composites for water adsorption heat transformation systems. *Industrial and Engineering Chemistry Research, 58*(47), 21493–21503. https://doi.org/10.1021/acs.iecr.9b04394

Huskić, I., Novendra, N., Lim, D. W., Topić, F., Titi, H. M., Pekov, I. V., Krivovichev, S. V., Navrotsky, A., Kitagawa, H., & Friščić, T. (2019). Functionality in metal-organic framework minerals: Proton conductivity, stability and potential for polymorphism. *Chemical Science,* *10*(18), 4923–4929. https://doi.org/10.1039/c8sc05088k

Institute for Health Metrics and Evaluation (IHME) (2021). Global Burden of Disease Study 2019 (GBD 2019) Results. Seattle. Retrieved May 19, 2023

Jiang, C., Sun, R., Du, Z., Singh, V., & Chen, S. (2020). A cationic Zr-based metal organic framework with enhanced acidic resistance for selective and efficient removal of CrO42-. *New Journal of Chemistry, 44*(29), 12646–12653. https://doi.org/10.1039/d0nj02279a

Kampouri, S., Ireland, C. P., Valizadeh, B., Oveisi, E., Schouwink, P. A., Mensi, M., & Stylianou, K. C. (2018). Mixed-phase MOF-derived titanium dioxide for photocatalytic hydrogen evolution: The impact of the templated morphology. *ACS Applied Energy Materials, 1*(11), 6541–6548. https://doi.org/10.1021/acsaem.8b01445

Kobielska, P. A., Howarth, A. J., Farha, O. K., & Nayak, S. (2018). Metal–organic frameworks for heavy metal removal from water. *Coordination Chemistry Reviews, 358*, 92–107. https://doi.org/10.1016/j.ccr.2017.12.010

Li, L., Xiang, S., Cao, S., Zhang, J., Ouyang, G., Chen, L., & Su, C. Y. (2013). A synthetic route to ultralight hierarchically micro/mesoporous Al (III)-carboxylate metal-organic aerogels. *Nature Communications, 4*, 1774–1779. https://doi.org/10.1038/ncomms2757

Li, R., Zhang, W., & Zhou, K. (2018). Metal–organic-framework-based catalysts for photoreduction of CO2. *Advanced Materials, 30*(35), 1–31. https://doi.org/10.1002/adma.201705512

Lin, Y., Weng, C., Tzeng, J., & Lin, Y. (2016). Adsorption and photocatalytic kinetics of visible-light response N-Doped TiO₂ nanocatalyst for indoor acetaldehyde removal under dark and light conditions. *International Journal of Photoenergy, 2016*, 3058429. https://doi.org/10.1155/2016/3058429

Lv, S. W., Liu, J. M., Li, C. Y., Zhao, N., Wang, Z. H., & Wang, S. (2019). A novel and universal metal-organic frameworks sensing platform for selective detection and efficient removal of heavy metal ions. *Chemical Engineering Journal, 375*, 122111. https://doi.org/10.1016/j.cej.2019.122111

Mahadi, N., Misran, H., Othman, S. Z., Jamaludin, N. S., Manap, A., & Anuar, N. F. S. (2015). Hydrothermal synthesis and characterizations of MOF-199 using renewable template. *Applied Mechanics and Materials, 773–774*(3), 226–231. https://doi.org/10.4028/www.scientific.net/amm.773-774.226

Mohan, A., De Jong, M. M., Poulios, I., Schropp, R. E. I., & Rath, J. K. (2015). Gas phase synthesis of two ensembles of silicon nanoparticles. *Journal of Physics D: Applied Physics, 48*(37), 375201. https://doi.org/10.1088/0022-3727/48/37/375201

Noraee, Z., Jafari, A., Ghaderpoori, M., Kamarehie, B., & Ghaderpoury, A. (2019). Use of metal-organic framework to remove chromium (VI) from aqueous solutions 03 chemical sciences 0306 physical chemistry (incl. structural). *Journal of Environmental Health Science and Engineering, 17*(2), 701–709. https://doi.org/10.1007/s40201-019-00385-8

Nuclear Energy Agency. (2015). *Handbook on Lead-bismuth Eutectic Alloy and Lead Properties, Materials Compatibility, Thermal- hydraulics and Technologies* (2015 edition). Nuclear Science.

Pakade, V. E., Tavengwa, N. T., & Madikizela, L. M. (2019). Recent advances in hexavalent chromium removal from aqueous solutions by adsorptive methods. *RSC Advances, 9*(45), 26142–26164. https://doi.org/10.1039/c9ra05188k

Pinto, M. L., Dias, S., & Pires, J. (2013). Composite MOF foams: The example of UiO-66/polyurethane. *ACS Applied Materials and Interfaces, 5*(7), 2360–2363. https://doi.org/10.1021/am303089g

Rajeshkumar, S., Liu, Y., Zhang, X., Ravikumar, B., Bai, G., & Li, X. (2018). Studies on seasonal pollution of heavy metals in water, sediment, fish and oyster from the Meiliang Bay of Taihu Lake in China. *Chemosphere, 191*, 626–638. https://doi.org/10.1016/j.chemosphere.2017.10.078

Rosli, S. A., Alias, N., Bashirom, N., Ismail, S., Tan, W. K., Kawamura, G., Matsuda, A., & Lockman, Z. (2021). Hexavalent chromium removal via photoreduction by sunlight on titanium–dioxide nanotubes formed by anodization with a fluorinated glycerol–water electrolyte. *Catalysts, 11*(3), 1–19. https://doi.org/10.3390/catal11030376

Santos-Lorenzo, J., San José-Velado, R., Albo, J., Beobide, G., Castaño, P., Castillo, O., Luque, A., & Pérez-Yáñez, S. (2019). A straightforward route to obtain zirconium-based metal-organic gels. *Microporous and Mesoporous Materials, 284*, 128–132.

Shaiful Bahari, A. M., Othman, S. Z., Mohamad Fadli, M. F., Zulkifli, M. Z. A., Biyamin, S. A., Islam, M. A., Aspanut, Z., Amin, N., & Misran, H. (2021a). Facile synthesis of Zr-based metal-organic gel (Zr-MOG) using "green" sol-gel approach. *Surfaces and Interfaces, 27*, 101469. https://doi.org/10.1016/j.surfin.2021.101469

Shaiful Bahari, A. M., Zulkifli, N. H., Azmin, A. N., Alias, N., Rosli, S. A., Sazalli, N. A. H., Lockman, Z., Amin, N., & Misran, H. (2021b). Facile synthesis of chloride-less zirconium-based metal- organic framework (MOF) as chromium (VI) removal via photoreduction. *Malaysian Journal of Microscopy*, 17(2), 220–238.

Shokouhfar, N., Aboutorabi, L., & Morsali, A. (2018). Improving the capability of UiO-66 for Cr(vi) adsorption from aqueous solutions by introducing isonicotinate: N -oxide as the functional group. *Dalton Transactions, 47*(41), 14549–14555. https://doi.org/10.1039/c8dt03196g

Torbina, V. V., Nedoseykina, N. S., Ivanchikova, I. D., Kholdeeva, O. A., & Vodyankina, O. V. (2019). Propylene glycol oxidation with hydrogen peroxide over Zr-containing metal-organic framework UiO-66. *Catalysis Today, 333*, 47–53. https://doi.org/10.1016/j.cattod.2018.11.063

Valvekens, P., Vermoortele, F., & De Vos, D. (2013). Metal-organic frameworks as catalysts: The role of metal active sites. *Catalysis Science and Technology, 3*(6), 1435–1445. https://doi.org/10.1039/c3cy20813c

Wani, P. A., Wani, J. A., & Wahid, S. (2018). Recent advances in the mechanism of detoxification of genotoxic and cytotoxic Cr(VI) by microbes. *Journal of Environmental Chemical Engineering, 6*(4), 3798–3807. https://doi.org/10.1016/j.jece.2018.05.042

Wen, J., Fang, Y., & Zeng, G. (2018). Progress and prospect of adsorptive removal of heavy metal ions from aqueous solution using metal–organic frameworks: A review of studies from the last decade. *Chemosphere, 201*, 627–643. https://doi.org/10.1016/j.chemosphere.2018.03.047

Wiktor, C., Meledina, M., Turner, S., Lebedev, O. I., & Fischer, R. A. (2017). Transmission electron microscopy on metal-organic frameworks-a review. *Journal of Materials Chemistry A, 5*(29), 14969–14989. https://doi.org/10.1039/c7ta00194k

Yang, F., Li, W., & Tang, B. (2018). Facile synthesis of amorphous UiO-66 (Zr-MOF) for supercapacitor application. *Journal of Alloys and Compounds, 733*, 8–14. https://doi.org/10.1016/j.jallcom.2017.10.129

Yang, Y., Wang, G., Peng, C., Deng, Q., Yu, Y., He, X., Hu, T., Jiang, L., Shan, S., Zheng, Y., Zhi, Y., & Su, H. (2023). Microwave-assisted synthesis of l-aspartic acid-based metal organic aerogel (MOA) for efficient removal of oxytetracycline from aqueous solution. *Applied Surface Science, 610*, 155608. https://doi.org/10.1016/j.apsusc.2022.155608

Zhao, J., Lee, D. T., Yaga, R. W., Hall, M. G., Barton, H. F., Woodward, I. R., Oldham, C. J., Walls, H. J., Peterson, G. W., & Parsons, G. N. (2016). Ultra-fast degradation of chemical warfare agents using MOF-nanofiber kebabs. *Angewandte Chemie-International Edition, 55*(42), 13224–13228. https://doi.org/10.1002/anie.201606656